ADVANCED ENERGY & SUSTAINABILITY RESEARCH
Open Access
www.advenergysustres.com

Light-Emitting Diode Visible-Light-Driven Photocatalytic Redox Reactions in Nitrogen Oxide Removal Using β-Bi_2O_3/Bi/g-C_3N_4 Prepared by One-Step In Situ Thermal Reduction Synthesis

Xing Qin, Huaqiao Tan, Yingnan Zhao, Sihang Cheng, Min Zhou, Jinliang Lin, Wing-Kei Ho, Haiwei Li, and Shun-Cheng Lee*

Traditional photocatalytic oxidation of nitrogen oxide (NO) may cause the more toxic NO_2 generation after longtime reaction, and even the ideal final production nitrate may also inevitably cause the poisoning of photocatalysts. Thus, utilizing photocatalytic reduction to remove NO into N_2 should be considered more practical but is still challenging currently. Herein, a novel S-scheme β-Bi_2O_3/Bi/g-C_3N_4 heterojunction photocatalyst is developed via a one-step in situ thermal reduction method. The photocatalytic degradation efficiency over this S-scheme photocatalyst exhibits around 88.7% degradation rate for NO with little NO_2 generation under light-emitting diode light irradiation, which is significantly higher than that of the pristine g-C_3N_4 (60%). Interestingly, both reduction of NO into N_2 and oxidation of NO into NO_3^- exist synchronously in the system. The increased degradation efficiency and the efficient reduction pathway occurring should be ascribed to the enhanced generation, separation, and transfer of the photogenerated carriers through the Bi-bridge S-scheme heterojunction. This study has provided a new route for regulating the photocatalytic reaction pathway for NO removal through a simple synthesis method.

1. Introduction

Excessive emission of nitrogen oxide (NO) has caused various environmental issues and health problems for decades.[1–3] Recently, utilizing photocatalysts to remove atmospheric NO has raised great attention thanks to its economic, environmentally friendly, and efficient properties.[4–7] However, massive researches only aim to improve the oxidation ability of photocatalysts through different modification methods.[8–11] Indeed, there are two main inherent problems of photocatalytic oxidation for NO removal that seriously restrict the actual application. First, the more toxic intermediated product nitrogen dioxide (NO_2) could be potentially generated during the longtime reaction. Second, the final ideal product nitrate (NO_3^-) could inevitably cause the poisoning of photocatalysts due to its coverage of the active site on the surface.[10,11] Based on these reasons, developing an efficient photocatalyst with strong reduction abilities to reduce NO into environmentally friendly nitrogen (N_2) directly should be more practicable and sustainable in actual application.

In recent years, because of the high position of conduction band (CB), unique adjustable electronic structure, metal-free, big specific surface area, and visible-light response, graphitic carbon nitride (g-C_3N_4) has been utilized for numerous photoreduction reactions, such as CO_2 reduction,[12–14] H_2 production,[15–17] and N_2 fixation.[18–20] Therefore, realizing NO reduction over g-C_3N_4 should be hypothetically feasible under proper conditions.[21] However, interestingly, g-C_3N_4 is normally designed for NO oxidation but not the reduction in numerous studies.[9] On the other hand, the pristine

X. Qin, H. Tan, M. Zhou, J. Lin, W.-K. Ho
Department of Science and Environmental Studies and the Centre for Environment and Sustainable Development (CESD)
The Education University of Hong Kong
Tai Po, N.T., Hong Kong, P. R. China
E-mail: keithho@eduhk.hk

The ORCID identification number(s) for the author(s) of this article can be found under https://doi.org/10.1002/aesr.202200157.

DOI: 10.1002/aesr.202200157

H. Tan, Y. Zhao, S. Cheng
Key Laboratory of Polyoxometalate Science of the Ministry of Education
Faculty of Chemistry
Northeast Normal University
Changchun 130024, P. R. China

W.-K. Ho
State Key Laboratory of Marine Pollution
City University of Hong Kong
Tat Chee Avenue, Kowloon, Hong Kong, P. R. China

H. Li, S.-C. Lee
Department of Civil and Environmental Engineering
The Hong Kong Polytechnic University
Hong Kong, P. R. China

$g\text{-}C_3N_4$ still has some inherent problems that greatly limit its application in NO removal, mainly including the high recombination rate of photogenerated carriers and the poor utilization of visible light.[22–24] Fortunately, constructing heterojunctions among suitable photocatalysts recently has been proven as one operative technique to improve the separation and transfer of photogenerated carriers and enhance the utilization of visible light.[25,26] Bismuth-based materials are regarded as green-metal-element photocatalysis because of their wide distribution and abundance in nature.[14] Thereinto, bismuth oxide (Bi_2O_3) has been applied in NO removal thanks to the excellent electrical conductivity, high stability, and visible light response.[27–29] Thus, it is reasonable to speculate that constructing a heterojunction between Bi_2O_3 and $g\text{-}C_3N_4$ could significantly inhibit the recombination of photogenerated carriers and enhance the absorption of visible light. Furthermore, the metallic Bi that in situ thermal reduced from Bi_2O_3 can also theoretically improve the NO removal efficiency over the $Bi_2O_3/g\text{-}C_3N_4$ photocatalyst because of the surface plasmon resonance (SPR) effect.[30,31]

Herein, a novel S-scheme $\beta\text{-}Bi_2O_3/Bi/g\text{-}C_3N_4$ heterojunction photocatalyst is successfully synthesized by a simple one-step in situ thermal reduction. The in situ thermal reduced metallic Bi can efficiently facilitate electron-carrier separation as a charge transfer bridge and enhance visible light absorption because of the SPR effect. Results revealed that the effective degradation of NO involved the reduction of NO into N_2 and oxidation of NO into NO_3^- synchronously. The improved performance can be ascribed to the enhanced generation, separation, and transfer of the photogenerated vital carriers. Detailed characterizations and photocatalytic performance of $\beta\text{-}Bi_2O_3/Bi/g\text{-}C_3N_4$ are then systematically studied.

2. Experimental Section

2.1. Synthesis

2.1.1. Materials

Bismuth nitrate pentahydrate ($Bi(NO_3)_3{\cdot}5H_2O$) and sodium borohydride ($NaBH_4$) were purchased from Sigma-Aldrich. Urea (CN_2H_4O) was purchased from Acros Organics. All chemicals used in this study were analytical grade without further purification. Distilled water was used throughout the experiments.

2.1.2. Preparation of $g\text{-}C_3N_4$ and $\beta\text{-}Bi_2O_3$

$g\text{-}C_3N_4$ (marked as CN) and $\beta\text{-}Bi_2O_3$ (marked as Bi_2O_3) were synthesized by placing 20 g urea and $Bi(NO_3)_3{\cdot}5H_2O$ into a crucible with cover respectively, and then burning in a muffle furnace under 600 °C for 3 h with a heating rate of 5 °C min^{-1} under the air atmosphere. Finally, the products were developed after cooling to room temperature.

2.1.3. Preparation of $\beta\text{-}Bi_2O_3/g\text{-}C_3N_4$

The $\beta\text{-}Bi_2O_3/g\text{-}C_3N_4$ (marked as BC) composite was synthesized by placing a certain amount of $Bi(NO_3)_3{\cdot}5H_2O$ (0.5, 0.75 and 1 g) and 20 g urea into a crucible and treated under continuous magnetic stirring at 180 °C by a heating agitator to make the mixtures evenly distributed. The crucible with mixtures was placed into a muffle furnace under 600 °C for 3 h with a heating rate of 5 °C min^{-1} under the air atmosphere. Finally, the $\beta\text{-}Bi_2O_3/g\text{-}C_3N_4$ composite was developed after cooling to room temperature. The $\beta\text{-}Bi_2O_3/g\text{-}C_3N_4$ photocatalyst with different weights of $Bi(NO_3)_3{\cdot}5H_2O$ was marked as BC-0.5, BC-0.75, and BC-1.

2.1.4. Preparation of $\beta\text{-}Bi_2O_3/Bi/g\text{-}C_3N_4$

The $\beta\text{-}Bi_2O_3/Bi/g\text{-}C_3N_4$ (marked as BBC) composite was synthesized as follows: approximately 0.4 g each of BC-0.5, BC-0.75, and BC-1 was placed into separate beakers that were added with 25 mL of distilled water and ultrasonically oscillated for 30 min. The metallic Bi was partially reduced out from $\beta\text{-}Bi_2O_3$ by adding 0.4 g of $NaBH_4$ into the beakers and stirring for 10 min without heating. Finally, the product was centrifuged and washed with distilled water followed by ethanol several times to remove $NaBH_4$. A series of the final product was marked as BBC-0.5, BBC-0.75, and BBC-1. BBC-0.75 showed the best photocatalytic degradation of NO in the series of BBC photocatalysts.

2.2. Characterization

The crystal phase structures were analyzed by X-ray diffraction (XRD: Bruker AXS D8 Focus with filtered Cu Kα radiation ($\lambda = 1.54056$ Å)), the scan range of 2θ was 5°–80°, and the scan rate was 0.01° 2θ/s. The morphologies and structures were obtained by scanning electron microscope (SEM: JEOL JSM 4800F) and transmission electron microscope (TEM: JEM-2100F microscope operated at 200 kV). The surface electronic states were analyzed by X-ray photoelectron spectroscopy (XPS: ESCALABMKII spectrometer with an Al Kα (1486.6 eV) achromatic X-ray source). The Brunauer–Emmett–Teller (BET) special surface area was measured at 77 K by a nitrogen adsorption–desorption isotherm device (ASAP 2020). The spectra and transient lifetime of photoluminescence (PL) were analyzed on a spectrometer (Horiba Jobin Yvon Fluorolog-3) with a QY accessory and a time-correlated single-photon counting lifetime spectroscopy system. Fourier transform infrared spectroscopy (FT-IR) was obtained using a Nicolet iS10 FT-IR spectrometer. C and N contents were tested by a Vario EL elemental analyzer. The ultraviolet–visible diffuse reflectance spectra (UV–vis DRS) were analyzed on a Shimadzu UV 2600 UV/vis spectrophotometer with $BaSO_4$ as a reference. The electrochemical performances were analyzed by a CHI660E Electrochemical Workstation in a standard three-electrode cell using a Pt plate, Ag/AgCl electrode, and sample deposited fluoride-tin oxide (FTO) as the counter electrode, reference electrode, and working electrode, respectively (CH Instruments, China).

2.3. Photocatalytic Activity Measurement

The photocatalytic activities of the as-prepared photocatalysts were evaluated through the photodegradation of NO at the parts per billion (ppb) level in a continuous flow rectangular reactor at ambient temperature. The volume of the reactor composed

of stainless steel and covered with quartz glass was 4.5 L ($L \times W \times H$, 30 cm × 15 cm × 10 cm). A light-emitting diode (LED) lamp with LOPB-30D model (SUNSHINE Light Company, Hong Kong, China) was used as the light source. The detailed information of the LED lamp are: size (154 × 107 × 31 mm); watt (30 W); color temperature (daylight 6500 K); light wavelength (mainly at 448 nm); lumen (2250 lm); and color rendering index (80). The LED lamp was vertically set above the reactor, and the distance was approximately 6.5 cm from the sample surface to the lamp. The light intensity of the LED lamp on the sample surface is approximately 60 500 lux (detected by PM6612 digital lux meter, PEAKMETER). About 0.3 g of the as-prepared photocatalyst was added into 30 mL of H_2O and ultrasonicated for 30 min. Then the mixed suspension was coated on a glass dish with a diameter of 11.5 cm and heated at 60 °C on a heater to completely evaporate the H_2O from the suspension. The dish with photocatalyst (the thickness of photocatalyst is approximately 1 mm for 0.3 g sample) was set into the reactor after cooling to room temperature. NO gas was introduced from a compressed gas cylinder containing the concentration of 20 parts per million (ppm) of NO (balanced with helium) in accordance with the traceable standard recommended by the National Institute of Standards and Technology. The initial concentration of NO was diluted to approximately 600 ppb by air stream supplied from a zero-air generator (Advanced Pollution Instrumentation, Teledyne Technologies Company, Model 701, USA) or an ultrahigh purity grade helium or nitrogen (99.999% min.) in the compressed gas cylinder via mass flow controllers (SIERRA SmartTrak 100 Series, The Netherlands). The gas streams were completely premixed in a gas blender, and the flow rate was controlled at 500 mL min^{-1} by a mass flow controller. The humidity of the gas streams was controlled by initially pumping the air stream into a humidifier with water before NO dilution. Except for the experiment of relative humidity (RH) study, all the photocatalytic activities were performed under approximately 50% (50 ± 5%) RH. After the adsorption–desorption equilibrium was achieved, the lamp was turned on for one cycle reaction (30 min) and then closed. For the successive photocatalytic reaction, the light lamp was reopen for 30 min after the adsorption–desorption equilibrium of NO at approximately 600 ppb was achieved again. One whole successive photocatalytic reaction included eight cycles in total. The NO concentration was continuously measured using a chemiluminescence NO_x analyzer (Advanced Pollution Instrumentation, Teledyne Technologies, Model T200) that can be used to monitor the concentrations of NO, NO_2, and NO_x ($NO_x = NO + NO_2$) at a sampling rate of 500 mL min^{-1}. The removal ratio (η) of NO was calculated as $\eta\ (\%) = (1 - C/C_0) \times 100$, where C and C_0 were the concentrations of NO in the outlet and initial feeding streams, respectively.

Active species trapping experiments were carried out to investigate the photocatalytic removal mechanism of NO over BBC-0.75 under the air atmosphere. KI, potassium dichromate ($K_2Cr_2O_7$), *tert*-butyl alcohol (TBA), and *p*-Benzoquinone (*p*-Ben) were chosen as scavengers for photogenerated holes, electrons, hydroxide radical (•OH), and superoxide radical ($\bullet O_2^-$), respectively. BBC-0.75 (0.3 g) with different trapping agents was added into 30 mL of H_2O and ultrasonically dispersed for 30 min. The aqueous suspension was equally coated onto a glass dish and dried at 60 °C in a heater to completely evaporate H_2O. Finally, the glass dish was used to test for the LED light photocatalytic activity.

3. Results and Discussion

3.1. Chemical Compositions

The composition and phase structure of the as-prepared photocatalysts were investigated through XRD (**Figure 1**a). The diffraction peaks at $2\theta = 13.1°$ and 27.5° can be attributed to the (100) and (002) phases of g-C_3N_4, respectively. The former was ascribed to the long-range interplanar stacking of aromatic systems, and the latter was ascribed to the in-plane structural packing motif. After calcination with $Bi(NO_3)_3{\cdot}5H_2O$, the two diffraction peaks at $2\theta = 30.1°$ and 32.5° were observed and were attributed to the (002) and (220) phases of β-Bi_2O_3 (standard car: PDF#45-1344), respectively. Following the increase in β-Bi_2O_3 doping content, the diffraction peak of β-Bi_2O_3 became sharper, revealing that the β-Bi_2O_3 was successfully doped into g-C_3N_4 (Figure S1, Supporting Information). Furthermore, after the in situ thermal reduction through $NaBH_4$, the diffraction peaks at $2\theta = 38.0°$ and 39.8° of BBC-0.75 appeared clearly. They were attributed to the (104) and (110) phases of metallic Bi (standard car: PDF#44-1246), respectively. The diffraction peaks of β-Bi_2O_3 in BBC-0.75 were reduced and hidden, which was ascribed to the crystallinity decreasing after the in situ thermal reduction. In short, XRD implied that β-Bi_2O_3 was successfully introduced into g-C_3N_4 and metallic Bi was successfully in situ grown on β-Bi_2O_3. The chemical structures of the as-prepared photocatalysts were confirmed by the Fourier transform infrared (FT-IR) spectroscopy spectra (Figure 1b). The absorption peaks between 1242 and 1637 cm^{-1} were ascribed to the C–N heterocycle stretching vibration, and the absorption peak at 808 cm^{-1} was explained to the band breathing mode of the triazine units of g-C_3N_4.[32] The peaks at 531 and 592 cm^{-1} were associated with the Bi–O vibration of BiO_6 units, while the band at 1391 cm^{-1} was assigned to the Bi–O stretching modes.[33,34] For BBC-0.75, the peak intensities corresponding to g-C_3N_4 became weaker within 531–592 cm^{-1} at 808 and 1391 cm^{-1} because of the synergistic effect after the modification with β-Bi_2O_3.[34] This result showed the effect of introducing β-Bi_2O_3 into g-C_3N_4 without chemical structure destruction, and this phenomenon was further confirmed in Figure S2, Supporting Information.

XPS measurement was applied to analyze the detailed chemical compositions of the as-prepared photocatalysts. The low-resolution XPS survey spectrum indicated that BBC-0.75 consisted of Bi, C, N, and O (Figure S3, Supporting Information). In Figure 1c, the peaks of BBC-0.75 at 157.8 and 163.2 eV were ascribed to the metallic Bi, and those at 158.3 and 163.7 eV were explained to Bi^{3+} in β-Bi_2O_3. The appearance of the peaks at 160.6 and 166.1 eV should be classified into the satellite peak of bismuth. In Figure 1d, the peaks at 527.5, 528.9, and 530.3 eV of BBC-0.75 can be ascribed to the O of adsorbed H_2O, the lattice oxygen atoms of β-Bi_2O_3, and the adsorbed O_2, respectively. Moreover, the peak at 532.3 eV can be ascribed to O in oxygen-deficient regions caused by reduction through $NaBH_4$.[35] In Figure 1e, the peaks at 284.8 and

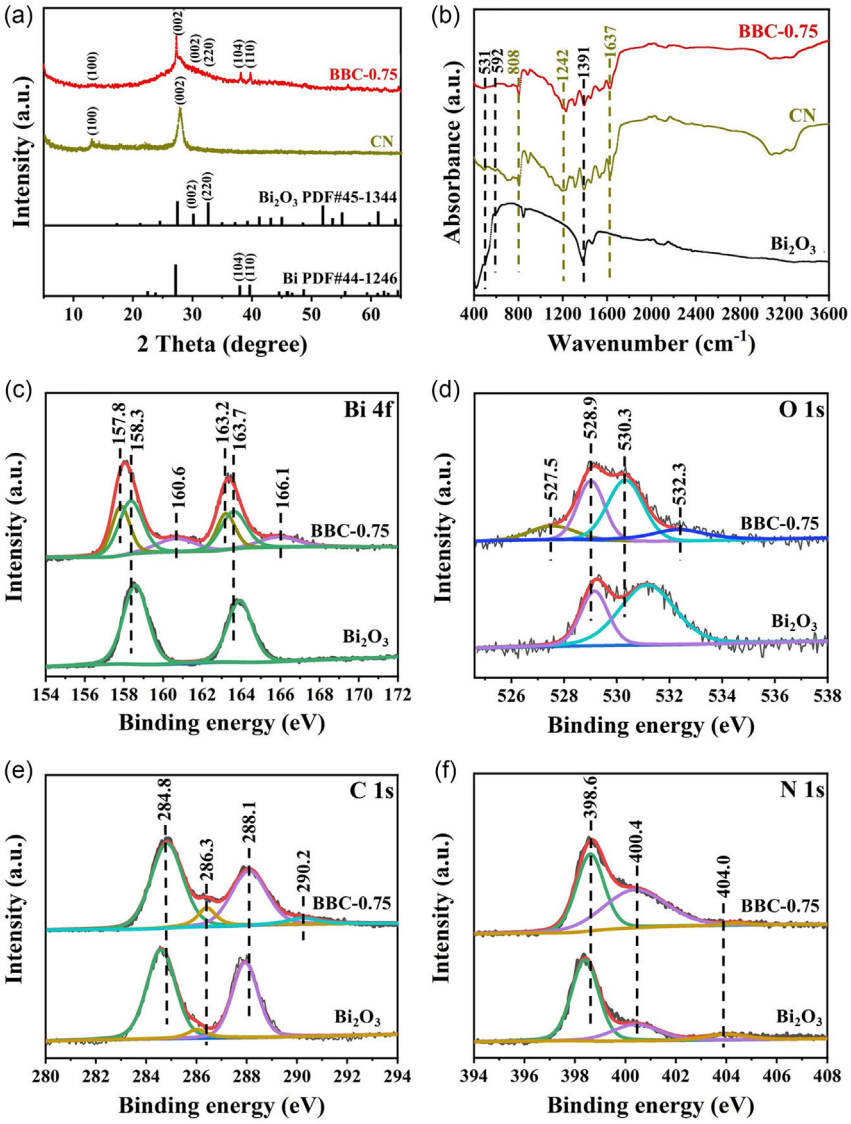

Figure 1. a) XRD patterns, b) FT-IR spectroscopy spectra, high-resolution XPS spectra of c) Bi 4*f*, d) O 1s, e) C 1s, and f) N 1s of the as-prepared photocatalysts.

288.1 eV of BBC-0.75 were attributed to the sp^2-bonded carbon (N—C═N) and C—N_3 bonds of g-C_3N_4, respectively. The peak at 286.3 eV was ascribed to the C—O bonding, and the peak at 290.2 eV was explained to the charging effect.[36,37] In Figure 1f, the peaks at 398.6, 400.4, and 404.0 eV of BBC-0.75 were ascribed to the tertiary N bonded to carbon atoms (N(–C)$_3$), the sp^2-hybridized aromatic N atoms bonded to carbon in the format of C—N═C, and the charging effects, respectively. Remarkably, the peak of BBC-0.75 showed a slight shift toward the low-energy status compared with that of Bi_2O_3, and showed a slight shift toward the high-energy status compared with that of g-C_3N_4. This unique phenomenon could be attributed to the S-scheme heterojunction but not the type II heterojunction.[38–40] Compared with the type II heterojunction, the S-scheme heterojunction can build a conductive medium inside or form an internal electric field to consume the unprofitable electrons and holes, therefore retaining those with more vital redox ability.[41–43]

3.2. Morphological Structure

The typical morphology and microstructure of BBC-0.75 were investigated through scanning electron microscopy (SEM) and transmission electron microscopy (TEM). The loose aggregated and lamellar structure with multiporous is shown in **Figure 2**a,b. Figure 2c reveals that the metallic Bi was in situ thermal reduced from β-Bi_2O_3 and had a close interface with β-Bi_2O_3 and g-C_3N_4. The lattice fringes with *d*-spacings of approximately 0.24 and 0.27 nm are shown in Figure 2d, which could be indexed as the (110) planes of the metallic Bi and the (220) planes of β-Bi_2O_3, respectively. The lattice fringes were also consistent with

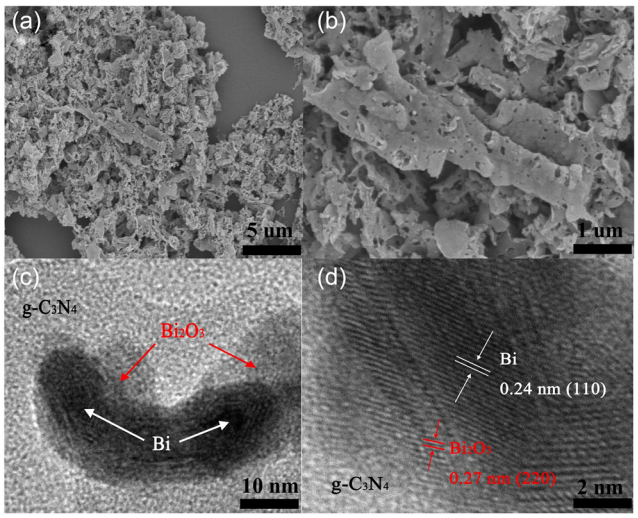

Figure 2. a,b) SEM images, and c,d) TEM images of BBC-0.75.

XRD analysis. In brief, the in situ thermal reduced metallic Bi, β-Bi_2O_3, and g-C_3N_4 were synthesized and closely connected in BBC-0.75. The selected energy-dispersive X-ray analysis (EDXA) elemental maps of BBC-0.75 shown in **Figure 3** confirmed that BBC-0.75 was composed of N, C, Bi, and O. The distribution of Bi and O was narrower than that of C and N, which revealed that both the in situ thermal reduced metallic Bi and β-Bi_2O_3 were almost wrapped in g-C_3N_4. This tight core–shell structure among the β-Bi_2O_3, the in situ thermal reduced metallic Bi, and g-C_3N_4 could effectively facilitate the separation of the photogenerated carriers.

The specific surface area (S_{BET}) and porous structures of the as-prepared photocatalysts were measured on N_2 adsorption–desorption equipment. Figure S4, Supporting Information, shows that all the as-prepared photocatalysts belonged to the isotherm of type IV with an H3 hysteresis loop except for β-Bi_2O_3. The calculated pore size distribution based on the density-functional theory (DFT) method revealed that the pore sizes were not uniform (inset of Figure S4, Supporting Information). The S_{BET}, peak pore size, and total pore volume of the photocatalysts are also summarized in Table S1, Supporting Information. The S_{BET} of BBC-0.75 (52.746 $m^2 g^{-1}$) was smaller than that of g-C_3N_4 (72.424 $m^2 g^{-1}$), owing to the introduced β-Bi_2O_3 and the in situ thermal reduced metallic Bi that can slightly block the mesoporous of g-C_3N_4.

3.3. Optical Properties and Band Structure

The optical properties of the as-prepared photocatalysts were investigated through the UV–vis diffuse reflectance spectra (UV–vis DRS). **Figure 4**a shows that g-C_3N_4, β-Bi_2O_3, and BBC-0.75 mainly absorbed photon energy under 440, 450, and 465 nm, respectively. The optical absorptions of BBC-0.75 showed a slight redshift compared with those of g-C_3N_4 and β-Bi_2O_3 because of the constructed S-scheme heterojunctions. Furthermore, the in situ thermal reduced metallic Bi in BBC-0.75 could significantly enhance the absorbance intensities of the visible light region (450–800 nm) due to the SPR effect. The bandgap energy of the as-prepared photocatalysts can be evaluated by the formula $\alpha(h\nu) = A(h\nu - E_g)^{n/2}$, where α, h, ν, A, and E_g correspond to the absorption coefficient, Planck constant, light frequency, proportionality, and bandgap energy, respectively. n is decided by the type of the optical transition in a semiconductor ($n = 4$ for indirect transition, and $n = 1$ for direct transition), and the values of n for g-C_3N_4 and β-Bi_2O_3 are 4 and 1, respectively. By using this formula, the calculated E_g values of g-C_3N_4 and β-Bi_2O_3 were 2.82 and 2.76 eV, respectively (Figure 4b). The Mott–Schottky (MS) plots were used to investigate the CB and valence band (VB) of as-prepared photocatalysts (Figure 4c). The CB potentials of g-C_3N_4 and β-Bi_2O_3 in an aqueous solution were −1.12 and 0.07 V (vs NHE), respectively. According to the E_g obtained from the UV–vis DRS curves, the VB positions of g-C_3N_4 and β-Bi_2O_3 were approximately 1.70 and 2.83 V (vs NHE), respectively (Figure 4d).

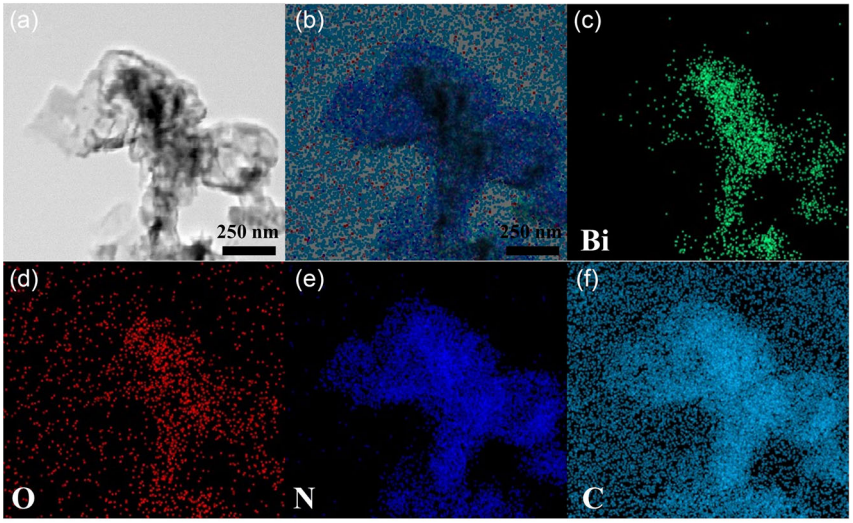

Figure 3. EDXA elemental maps of BBC-0.75.

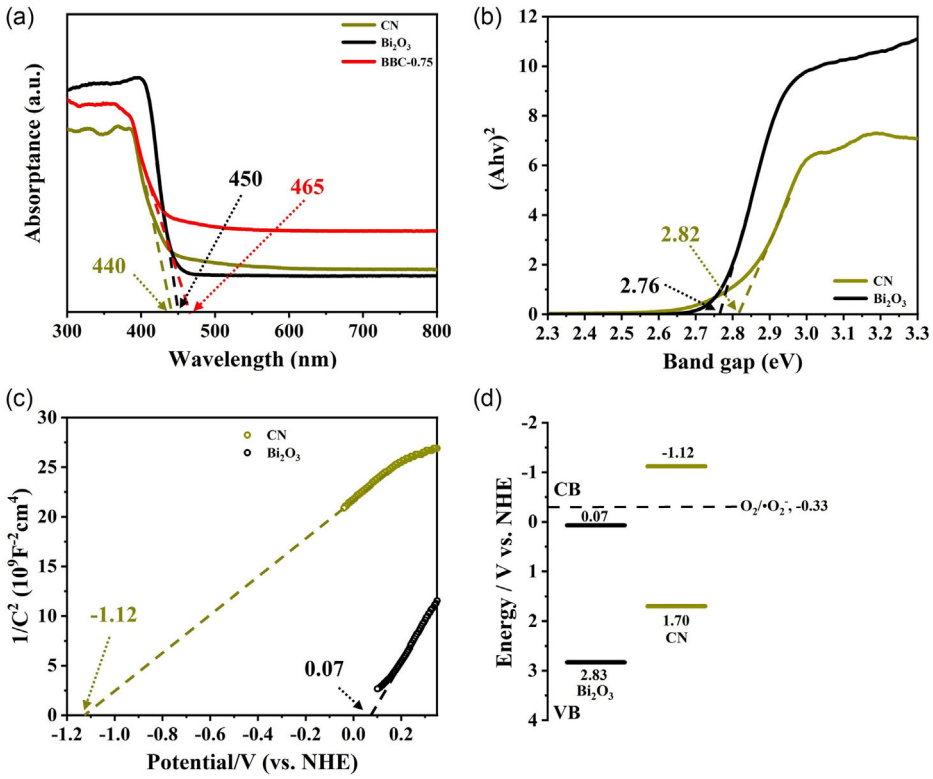

Figure 4. a) UV–vis DRS, b) electronic band structures, c) MS plot, and d) the energy positions of CB and VB of the as-prepared photocatalysts.

3.4. Charge Transfer Mechanism

The recombination rates of the photogenerated carriers of the as-prepared photocatalysts were evaluated using PL spectra. **Figure 5**a shows the PL spectra of the pristine g-C_3N_4, β-Bi_2O_3, and BBC-0.75 with an excitation wavelength at 330 nm. The PL spectrum peaks of g-C_3N_4, β-Bi_2O_3, and BBC-0.75 were at 452, 462, and 443 nm, respectively. This fluorescence emission was caused by the bandgap recombination of the photogenerated carriers. Compared with g-C_3N_4, BBC-0.75 showed a smaller PL spectrum peak, which can be ascribed to the incorporated β-Bi_2O_3 and the in situ thermal reduced metallic Bi that could significantly inhibit the recombination of the photogenerated carriers. The time-resolved fluorescence decay spectra at ns level were investigated, as shown in Figure 5b; the fluorescence decay kinetics for BBC-0.75 was smaller than that for g-C_3N_4. The radiative lifetime with different ratios can be calculated by fitting the decay spectra summarized in Table S2, Supporting Information. The short lifetime (τ_1) and long lifetime (τ_2) of BBC-0.75 were 2.3852 and 13.0094 ns, respectively, and both were smaller than those of g-C_3N_4 ($\tau_1 = 3.5976$ ns and $\tau_2 = 22.0035$ ns). The results suggested that the photogenerated carriers of BBC-0.75 were rapidly generated and separated, and quickly participated in the redox reaction on the surface thanks to the S-scheme heterojunction.

Transient photocurrent density was used to investigate the electronic interaction and the separation of the photogenerated carriers of the as-prepared photocatalysts. As shown in Figure 5c, the photocurrent intensity of BBC-0.75 was higher than that of g-C_3N_4 and β-Bi_2O_3, which was ascribed to the best photoelectric response ability of the photogenerated carriers due to the constructed in situ thermal reduced Bi-bridge S-scheme heterojunction. Electrochemical impedance spectroscopy (EIS) was employed further to determine the transfer efficiency of the photogenerated carriers. As shown in the EIS Nyquist plots (Figure 5d), BBC-0.75 reflected a similar Nyquist plot diameter to g-C_3N_4, which could be ascribed to the core–shell structure among the in situ thermal reduced metallic Bi, β-Bi_2O_3, and g-C_3N_4. g-C_3N_4 as the outer layer of the core–shell structure mainly influenced the transfer of photogenerated carriers.

3.5. Photocatalytic Activity and Stability

Compared with the traditional photocatalytic irradiation sources (such as xenon lamps and halogen lamps), LED lamps are recently considered more efficient in practical application thanks to the low energy consumption, high current-to-light conversion efficiency, high operational stability, low liberation of heat, widespread use, and inexpensive.[44–46] Thus, the photocatalytic removal efficiency over as-prepared photocatalysts was evaluated under the air atmosphere through LED light irradiation in a continuous reactor in this study.

The results in **Figure 6**a show the variation in NO concentrations (C/C_0, %) with irradiation time over the as-prepared photocatalysts. BBC-0.75 had the best degradation efficiency of NO (approximately 88.7%) and the most rapid degradation rate among the photocatalysts. The NO_2 intermediate was

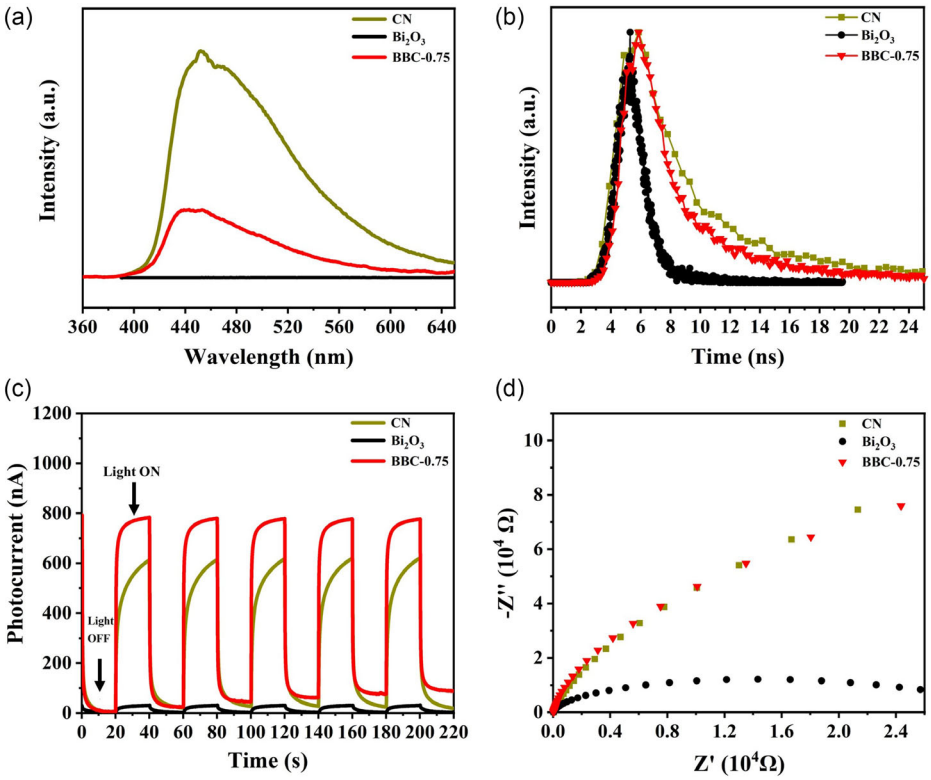

Figure 5. a) PL emission spectra, b) emission decay time, c) transient photocurrent density, and d) EIS spectra of the as-prepared photocatalysts.

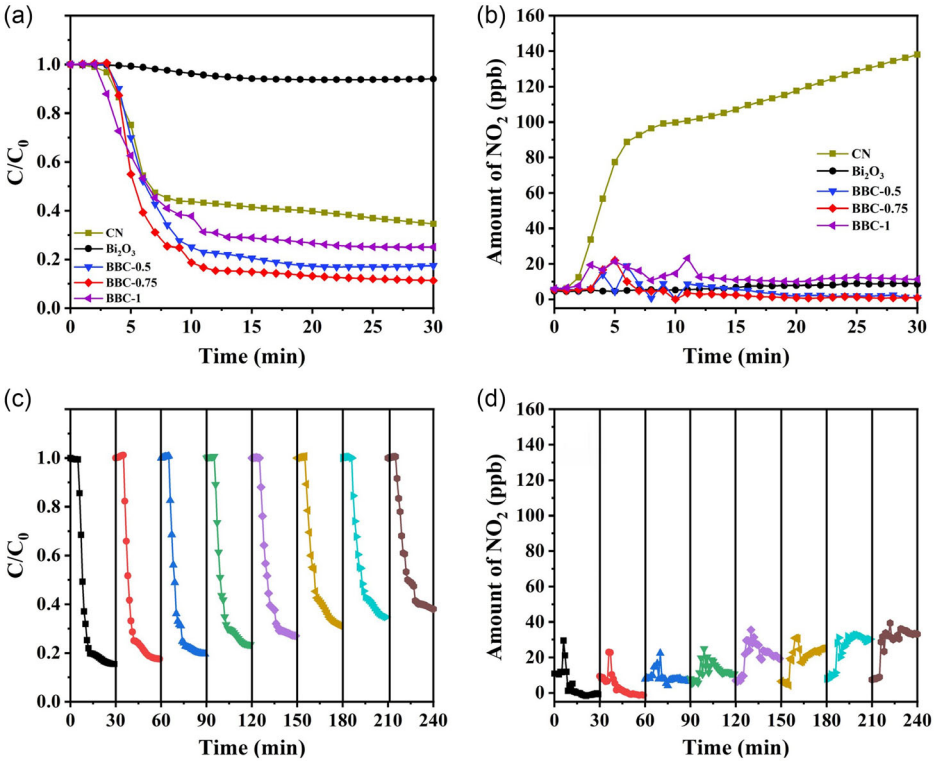

Figure 6. a,b) Photocatalytic removal of NO and the generated NO_2 intermediate during irradiation over as-prepared photocatalysts, c,d) stability test of NO degradation, and the generated NO_2 intermediate over BBC-0.75.

significantly inhibited during the reaction over BBC-0.75 compared to g-C_3N_4 (Figure 6b). These results could be ascribed to the construction of the Bi-bridge S-scheme heterojunction that can dramatically improve the generation and separation of the photogenerated carriers, thus enhancing the degradation efficiency and speeding up the reaction rate. Eight runs of the photocatalytic experiment under the air atmosphere were conducted under the same conditions to test the degradation efficiency stability over BBC-0.75. As shown in Figure 6c,d, the photocatalytic performance over BBC-0.75 was only slightly decreased without massive NO_2 generation after eight runs, indicating that the photodegradation efficiency of BBC-0.75 was acceptably stable. Interestingly, BC-0.75 can also have a higher NO degradation efficiency than g-C_3N_4 (Figure S5a,b, Supporting Information), but the removal efficiency was gradually decreased (Figure S5c, Supporting Information) and NO_2 intermediate was significantly increased during the irradiation over BC-0.75 (Figure S5d, Supporting Information). To further investigate the stability of BBC-0.75, the XRD analysis before and after the reaction over BBC-0.75 was also studied, as shown in Figure S7, Supporting Information. There was no significant structural change of BBC-0.75 before and after the successive photocatalytic reaction. Especially, the (104) and (110) phases of Bi were still clearly observed within the BBC-0.75 after the reaction, revealing that the metallic Bi could be stable in the S-scheme system as a photocarrier transfer bridge without photooxidizing. The removal efficiency of NO over BBC-0.75 under different RH conditions was also investigated, as shown in Figure S8, Supporting Information. Because of the competitive adsorption between H_2O and NO, the removal efficiency decreased following the RH increase. However, the generation of NO_2 intermediate was all inhibited under different RH conditions, revealing that BBC-0.75 could thoroughly oxidize NO into nitrate and reduce NO to N_2 even under variation RH conditions. In summary, compared with BC-0.75, the more excellent stability over BBC-0.75 revealed that nitrate that could significantly poison photocatalyst should not be massively produced during the reaction, and the small amount of NO_2 intermediate produced over BBC-0.75 also revealed that NO_2 was not the primary product. These results suggested that photoreduction may be involved during the NO photodegradation rather than the traditional full photooxidation thanks to the construction of Bi-bridge S-scheme heterojunction.

3.6. Photocatalytic Mechanism for NO Removal

Active species trapping experiments were carried out to investigate the photocatalytic removal mechanism of NO over BBC-0.75 under the air atmosphere. Potassium iodide (KI), $K_2Cr_2O_7$, TBA, and *p*-Ben were chosen as scavengers for photogenerated holes, electrons, hydroxide radical (•OH), and superoxide radical ($\bullet O_2^-$), respectively. As shown in **Figure 7**a, $K_2Cr_2O_7$ addition can almost absolutely depress NO removal over BBC-0.75, revealing that the photogenerated electrons were the main reactive species. Moreover, the addition of *p*-Ben can significantly depress

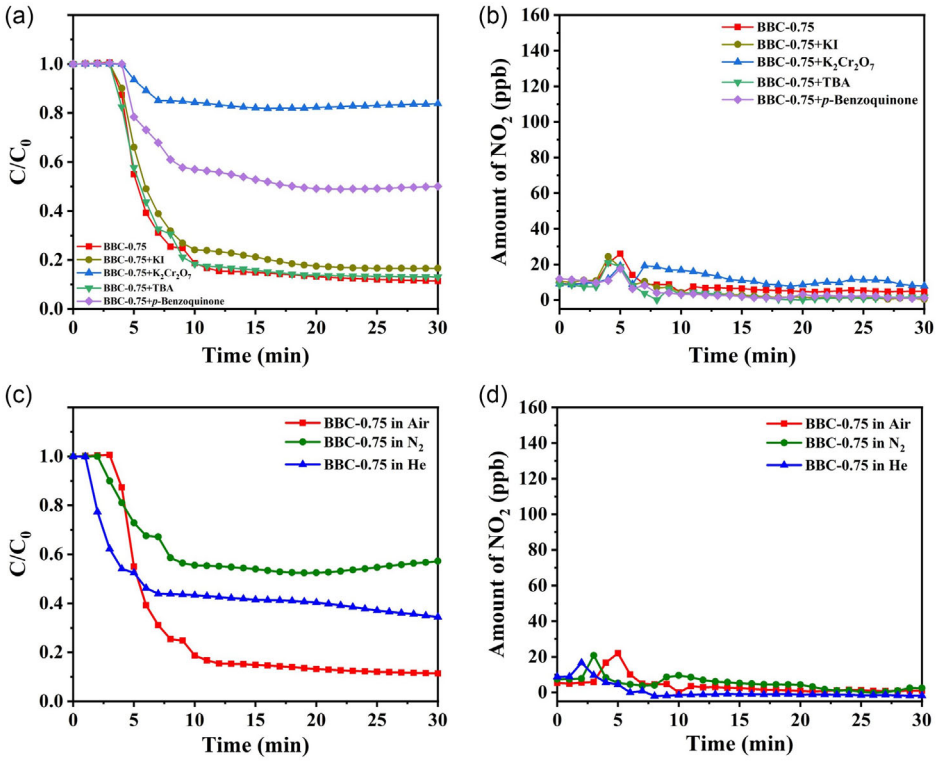

Figure 7. a) Photocatalytic removal of NO in the presence of different scavengers, b) the generated NO_2 intermediate in the presence of different scavengers, c) photocatalytic removal of NO under different atmospheres, and d) the generated NO_2 intermediate under different atmospheres over BBC-0.75.

NO removal over BBC-0.75, suggesting that $\bullet O_2^-$ was also a reactive species. On the other hand, the generated $\bullet O_2^-$ indicated that a Bi-bridge S-scheme heterojunction of BBC-0.75 was actually successfully constructed. If the photocarriers transfer of BBC-0.75 followed the type II heterojunction mechanism but not S-scheme, then $\bullet O_2^-$ should not be detected because of the inadequate oxidation potential of Bi_2O_3 (0.07 eV).[47,48] Interestingly, BBC-0.75 could still remove NO after trapping $\bullet O_2^-$, but the degradation efficiency was almost completely suppressed after trapping the photogenerated electrons. Remarkably, little NO_2 was generated after trapping $\bullet O_2^-$ and the photogenerated electrons (Figure 7b), revealing that NO was not oxidized into NO_2 by the environmental O_2 or the adding agents during the reaction. Thus, except for producing $\bullet O_2^-$ via an O_2 reduction, it is reasonable to speculate that part of the photogenerated electrons could directly participate in NO degradation over BBC-0.75. Given the strong reduction ability of the photogenerated electrons, some parts of NO may have been reduced by the photogenerated electrons directly. According to the previous literature, nitrogen is the possible main final product during NO reduction.[49,50] The comparison of the active species trapping experiments between g-C_3N_4 and BBC-0.75 was also investigated, as shown in Figure S9, Supporting Information. NO was mainly oxidized through $\bullet O_2^-$ radicals over g-C_3N_4 because of the complete inhibition of activity, and NO_2 intermediate was generated during the reaction over g-C_3N_4. Compared with g-C_3N_4, NO was both oxidized by $\bullet O_2^-$ radicals and reduced by electrons over BBC-0.75 without NO_2 intermediate generation, which should be ascribed to the more producing of $\bullet O_2^-$ radicals with stronger oxidation ability and photoelectrons with strong reduction ability, respectively, thanks to the Bi SPR effect and S-scheme construction.

The reduction pathway of NO degradation over BBC-0.75 was further investigated by replacing the compressed air carrier gas with ultrahigh-purity helium gas and nitrogen gas to achieve anaerobic and dry testing conditions, respectively. Interestingly, BBC-0.75 still showed approximately 60% and 45% degradation efficiency under helium gas and nitrogen gas, respectively (Figure 7c), which was significantly higher than that of BC-0.75 (Figure S6a, Supporting Information). NO_2 intermediate was also not generated after 30 min irradiation over both BBC-0.75 (Figure 7d) and BC-0.75 (Figure S6b, Supporting Information). These results further confirmed that the efficient reduction of NO during irradiation over BBC-0.75 should be ascribed to the improved separation and transfer of photogenerated carriers. Remarkably, the degradation efficiency of NO under nitrogen gas was lower than under helium gas over BBC-0.75 and BC-0.75. This phenomenon should be due to the nitrogen atmosphere that may inhibit the produced nitrogen desorbing from the active sites and lower the degradation efficiency of NO.

On the basis of the experimental results, characterizations, and analyses, a possible degradation mechanism of atmospheric NO under LED light irradiation over Bi-bridge S-scheme BBC-0.75 photocatalyst was proposed (**Figure 8**). Both g-C_3N_4 and β-Bi_2O_3 were excited after irradiation, and the photogenerated electrons and holes were located in their own CB and VB, respectively. Given the energy-level difference and tightly coupled metallic Bi bridge, the photogenerated electrons on

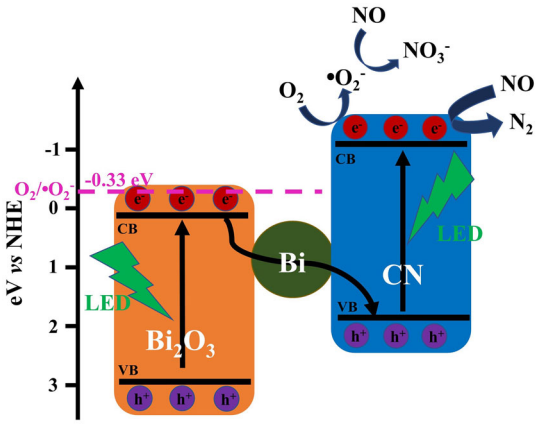

Figure 8. The potential degradation mechanism of NO under air atmosphere over BBC-0.75.

the CB of β-Bi_2O_3 could transfer to the VB of g-C_3N_4 and were annihilated with the holes of g-C_3N_4. Some parts of the strong reductive electrons on the CB of g-C_3N_4 in BBC-0.75 could reduce O_2 to $\bullet O_2^-$ radicals due to their more negative potential than E ($O_2/\bullet O_2^-$, −0.33 eV), and the $\bullet O_2^-$ radicals could further oxidize NO into NO_3^-. Some parts of the remaining electrons on the CB of g-C_3N_4 in BBC-0.75 could also reduce NO into N_2 directly because of their strong reduction ability. Thus, the enhanced photocatalytic degradation of NO and the reduction pathway occurring were ascribed to the unique Bi-bridge S-scheme heterojunction of BBC-0.75. This kind of heterojunction can realize the efficient generation and separation of photogenerated carriers and sufficiently inhibit their recombination.

4. Conclusion

A novel bismuth-bridge S-scheme β-Bi_2O_3/Bi/g-C_3N_4 heterojunction photocatalyst was developed via a one-step in situ thermal reduction method. Compared with g-C_3N_4 and β-Bi_2O_3 photocatalysts, the β-Bi_2O_3/Bi/g-C_3N_4 photocatalyst exhibited the highest photocatalytic performance toward NO degradation with little NO_2 generation in the atmosphere. Both the reduction and oxidation pathways of NO occurred synchronously during LED light irradiation over the β-Bi_2O_3/Bi/g-C_3N_4 photocatalyst, and the main reactive species involved are the photogenerated electrons and $\bullet O_2^-$ radicals. This improved degradation efficiency and photoreduction existing over β-Bi_2O_3/Bi/g-C_3N_4 photocatalyst were ascribed to the improved generation, separation, and transfer of photogenerated carriers through the Bi-bridge S-scheme heterojunction. Instead of the traditional fully photocatalytic oxidation of NO that may cause the final products to poison the photocatalyst, the efficient and economical method presented in this study may open a new opportunity for degrading the atmosphere's low level of NO into environmentally friendly N_2.

Supporting Information

Supporting Information is available from the Wiley Online Library or from the author.

Acknowledgements

This work was financially supported by the National Key Research and Development Program of China (grant no. 2016YFA0203000). This research was also supported by the General Research Fund, Research Grants Council of Hong Kong Government (project nos. 18301117 and 18300920) and Dean's Research Fund (04638), FLASS, EdUHK.

Conflict of Interest

The authors declare no conflict of interest.

Data Availability Statement

The data that support the findings of this study are available from the corresponding author upon reasonable request.

Keywords

bismuth, graphitic carbon nitride, light-emitting diodes (LEDs), nitrogen oxide (NO) degradation, S-scheme heterojunctions

Received: October 7, 2022
Revised: November 16, 2022
Published online: November 30, 2022

[1] A. Richter, J. P. Burrows, H. Nüß, C. Granier, U. Niemeier, *Nature* **2005**, *437*, 129.
[2] M. Kampa, E. Castanas, *Environ. Pollut.* **2008**, *151*, 362.
[3] E. A. Davidson, *Nat. Geosci.* **2009**, *2*, 659.
[4] Y. Sun, E. Zwolińska, A. G. Chmielewski, *Environ. Sci. Technol.* **2016**, *46*, 119.
[5] C. Li, Y. Xu, W. Tu, G. Chen, R. Xu, *Green Chem.* **2017**, *19*, 882.
[6] Y. Boyjoo, H. Sun, J. Liu, V. K. Pareek, S. Wang, *Chem. Eng. J.* **2017**, *310*, 537.
[7] J. Lin, W. Ho, X. Qin, C. F. Leung, V. K. M. Au, S. Cheng Lee, *Small.* **2022**, *18*, 2105484.
[8] J. Lasek, Y. H. Yu, J. C. S. Wu, *J. Photochem. Photobiol. C Photochem. Rev.* **2013**, *14*, 29.
[9] A. Nikokavoura, C. Trapalis, *Appl. Surf. Sci.* **2018**, *430*, 18.
[10] V. H. Nguyen, B. S. Nguyen, C. W. Huang, T. T. Le, C. C. Nguyen, T. T. Nhi Le, D. Heo, Q. V. Ly, Q. T. Trinh, M. Shokouhimehr, C. Xia, S. S. Lam, D. V. N. Vo, S. Y. Kim, Q. Van Le, *J. Cleaner Prod.* **2020**, *270*, 121912.
[11] M. Zhou, H. Ou, S. Li, X. Qin, Y. Fang, S. Lee, X. Wang, W. Ho, *Adv. Sci.* **2021**, *8*, 2102376.
[12] J. Fu, B. Zhu, C. Jiang, B. Cheng, W. You, J. Yu, *Small.* **2017**, *13*, 1603938.
[13] S. Ye, R. Wang, M. Z. Wu, Y. P. Yuan, *Appl. Surf. Sci.* **2015**, *358*, 15.
[14] R. Mohan, *Nat. Chem.* **2010**, *2*, 336.
[15] R. Shen, K. He, A. Zhang, N. Li, Y. H. Ng, P. Zhang, J. Hu, X. Li, *Appl. Catal. B Environ.* **2021**, *291*, 120104.
[16] D. Ruan, S. Kim, M. Fujitsuka, T. Majima, *Appl. Catal. B Environ.* **2018**, *238*, 638.
[17] L. Kong, Y. Ji, Z. Dang, J. Yan, P. Li, Y. Li, S. F. Liu, *Adv. Funct. Mater.* **2018**, *28*, 1800668.
[18] S. Cao, B. Fan, Y. Feng, H. Chen, F. Jiang, X. Wang, *Chem. Eng. J.* **2018**, *353*, 147.
[19] X. Yu, S. F. Ng, L. K. Putri, L. L. Tan, A. R. Mohamed, W. J. Ong, *Small.* **2021**, *17*, 2006851.
[20] W. Wang, H. Zhou, Y. Liu, S. Zhang, Y. Zhang, G. Wang, H. Zhang, H. Zhao, *Small.* **2020**, *16*, 1906880.
[21] J. Zhu, Y. Wei, W. Chen, Z. Zhao, A. Thomas, *Chem. Commun.* **2010**, *46*, 6965.
[22] J. Ma, C. Wang, H. He, *Appl. Catal. B Environ.* **2016**, *184*, 28.
[23] J. Fu, J. Yu, C. Jiang, B. Cheng, *Adv. Energy Mater.* **2018**, *8*, 1701503.
[24] H. Wang, W. He, X. Dong, H. Wang, F. Dong, *Sci. Bull.* **2018**, *63*, 117.
[25] N. Tian, H. Huang, C. Liu, F. Dong, T. Zhang, X. Du, S. Yu, Y. Zhang, *J. Mater. Chem. A* **2015**, *3*, 17120.
[26] J. Low, J. Yu, M. Jaroniec, S. Wageh, A. A. Al-Ghamdi, *Adv. Mater.* **2017**, *29*, 1601694.
[27] J. Nie, G. Zhu, W. Zhang, J. Gao, P. Zhong, X. Xie, Y. Huang, M. Hojamberdiev, *Chem. Eng. J.* **2021**, *424*, 130327.
[28] B. Lei, W. Cui, J. Sheng, H. Wang, P. Chen, J. Li, Y. Sun, F. Dong, *Sci. Bull.* **2020**, *65*, 467.
[29] Y. Lu, Y. Huang, Y. Zhang, J. Cao, H. Li, C. Bian, S. C. Lee, *Appl. Catal. B Environ.* **2018**, *231*, 357.
[30] F. Dong, Z. Zhao, Y. Sun, Y. Zhang, S. Yan, Z. Wu, *Environ. Sci. Technol.* **2015**, *49*, 12432.
[31] Y. Cui, M. Li, N. Zhu, Y. Cheng, S. S. Lam, J. Chen, Y. Gao, J. Zhao, *Nano Today.* **2022**, *43*, 101432.
[32] H. Li, H. Zhao, Y. Dong, Y. Zhu, J. Li, *Adv. Energy Sustainability Res.* **2022**, *3*, 2200116.
[33] T. H. T. Vinh, C. M. Thi, P. Van Viet, *Mater. Lett.* **2020**, *281*, 128637.
[34] K. R. S. Devi, S. Mathew, R. Rajan, J. Georgekutty, K. Karthik, D. Pinheiro, S. Sugunan, *Appl. Surf. Sci.* **2019**, *494*, 465.
[35] D. Chen, S. Wu, J. Fang, S. Lu, G. Y. Zhou, W. Feng, F. Yang, Y. Chen, Z. Q. Fang, *Sep. Purif. Technol.* **2018**, *193*, 232.
[36] J. Huang, D. Li, R. Li, Q. Zhang, T. Chen, H. Liu, Y. Liu, W. Lv, G. Liu, *Chem. Eng. J.* **2019**, *374*, 242.
[37] M. Vu, M. Sakar, C. Nguyen, T. Do, *ACS Sustainable Chem. Eng.* **2018**, *6*, 4194.
[38] K. Xiao, T. Wang, M. Sun, A. Hanif, Q. Gu, B. Tian, Z. Jiang, B. Wang, H. Sun, J. Shang, P. K. Wong, *Environ. Sci. Technol.* **2020**. *54*, 537.
[39] Q. Xu, L. Zhang, B. Cheng, J. Fan, J. Yu, *Chem* **2020**, *6*, 1543.
[40] F. Xu, K. Meng, B. Cheng, S. Wang, J. Xu, J. Yu, *Nat. Commun.* **2020**, *11*, 1.
[41] J. Wen, J. Xie, X. Chen, X. Li, *Appl. Surf. Sci.* **2017**, *391*, 72.
[42] K. Qi, B. Cheng, J. Yu, W. Ho, *Chinese J. Catal.* **2017**, *38*, 1936.
[43] Q. Xu, L. Zhang, J. Yu, S. Wageh, A. A. Al-Ghamdi, M. Jaroniec, *Mater. Today* **2018**, *21*, 1042.
[44] M. Izadifard, G. Achari, C. H. Langford, *Catalysts* **2013**, *3*, 726.
[45] A. Abdelhaleem, W. Chu, X. Liang, *Appl. Catal. B Environ.* **2019**, *244*, 823.
[46] T. Li, A. Abdelhaleem, W. Chu, S. Pu, F. Qi, J. Zou, *Chem. Eng. J.* **2021**, *411*, 128450.
[47] Y. Bao, S. Song, G. Yao, S. Jiang, *Sol. RRL* **2021**, *5*, 2100118.
[48] P. Xia, S. Cao, B. Zhu, M. Liu, M. Shi, J. Yu, Y. Zhang, *Angew. Chem. Int. Ed.* **2020**, *59*, 5218.
[49] Q. Wu, R. Van De Krol, *J. Am. Chem. Soc.* **2012**, *134*, 9369.
[50] G. Dong, D. L. Jacobs, L. Zang, C. Wang, *Appl. Catal. B Environ.* **2017**, *218*, 515.